A numerical hydrodynamic study of the influence of prolate and prolate 45-degrees ellipsoids on laminar flow

H.R. Díaz-Ojeda,[1] Yifu Zhang (张一夫),[2] Stephen Turnock,[2] and Julio Pérez-Sánchez[1]
[1)] *Universidad de Las Palmas de Gran Canaria (ULPGC), Las Palmas de Gran Canaria, 35001, Spain*
[2)] *Maritime Engineering, University of Southampton, Boldrewood Campus, Southampton, SO16 7QF, Hampshire, United Kingdom*

(*Electronic mail: hectorruben.diaz@ulpgc.es and yifu.zhang@soton.ac.uk)

This paper examines the impact of two tandem configurations of ellipsoids on laminar flow using numerical methods. The first configuration features an ellipsoid in a prolate orientation, while the other employs a prolate ellipsoid tilted at a 45º angle relative to the vertical axis. The study investigates inter-ellipsoid distances ranging from one ellipsoid diameter (1D) to eight diameters (8D) from the ellipsoids' centers and different Reynolds numbers (100, 200, 300, and 400). The presented results focus on hydrodynamic forces, wake symmetry, and wake patterns for different scenarios. The findings reveal that when an angle is present in the ellipsoid, the drag forces between the front and rear ellipsoids tend to approach at smaller separations compared to the prolate orientation case. In these cases, flow separation is asymmetric in the x-y plane but becomes symmetric in the x-z plane at larger ellipsoid spacings. Additionally, the detachment zones are analyzed concerning the angle and Reynolds number. It is observed that up to a distance of approximately 4D, the wake of the front ellipsoid significantly influences the recirculation and hydrodynamics of the rear ellipsoid.

I. INTRODUCTION

The flow over bluff bodies has been of great interest in many fields. Initially explored through experimental studies, which were gradually complemented by theoretical approaches, this area of research has now advanced to extensively utilize Computational Fluid Dynamics (CFD) techniques. These studies, which typically account for the viscous effects of the flow, serve as benchmarks and foundational references for investigating more complex flows and structures in real-world scenarios. In general, most studies focus on cylinders[1], spheres[2],[3], and non-rounded shapes such as plates[4] or rectangles[5] due to their relevance in engineering, biological, and other applications. Additionally, some studies focus on pinned structures[6], proximity to walls, and interactions between structures. Concerning the proximity between structures, the most commonly investigated arrangements are side-by-side and tandem configurations. These configurations are prevalent in engineering designs involving multiple body interactions, such as bridges crossing long rivers, buildings[7], or real situations like multiple runners in a race[8].

Regarding the current research, initial studies on rounded bodies focused on spheres, conducted experimentally by[9] and[10]. These studies highlighted the complex nature of flow detachment related to viscous effects and Reynolds numbers. Such factors significantly influence the drag on the sphere and its associated shedding frequency. In summary, various flow regimes have been identified around a single sphere—subcritical, critical, supercritical, and transcritical[9]—primarily determined by the Reynolds number and specific conditions affecting the body. Over time, theoretical studies have broadened our understanding of these bluff bodies. For example,[11] investigated the dynamics of a sphere moving through a tube. With advancements in computational technology, a substantial body of CFD research now supplements these experimental findings, examining a wide range of Reynolds numbers and providing detailed analyses of vorticity fields, streamlines, and pressure distributions around the sphere[12]. Analyzing low Reynolds numbers for this geometry,[10] and[13] examined the wake configuration behind a sphere. They demonstrated that for $Re < 24$, there is no flow separation; the flow remains steady and axisymmetric.[13] further observed that the angle of separation increases beginning at Reynolds 60, intensifying as this number rises.[14] categorized the wake into six distinct classes based on the Reynolds number. The authors also noted that at very low Reynolds numbers, the flow exhibits pronounced symmetry. As the Reynolds number increases, the flow begins to separate, and the length of the wake increases. The flow transitions from axisymmetric to non-axisymmetric when the Reynolds number reaches approximately 210 to 212[14–17]. In this regime, the flow features two vortical tails that, although of opposite sign, have similar structures and exhibit planar symmetry. Increasing the Reynolds number further triggers a transition from steady to time-dependent planar symmetry. This instability occurs within the Reynolds number range of 270 to 290[15,18–20]. During this phase, the flow becomes unsteady and periodic, characterized by a single dominant frequency. At a Reynolds number of 300,[21] notes the periodicity of the vortex, a finding supported by recent numerical studies[19,22]. Using direct numerical simulation across Reynolds numbers from 25 to 1000,[19] demonstrates that planar symmetry evolves into a chaotic state for Reynolds numbers between 300 and 500. Further,[22] finds the flow at $Re = 300$ to be unsteady and time-dependent, characterized by regular flow separation fluctuations. The research also indicates that flow separation remains very stable for $Re < 200$, but becomes unsteady, non-periodic, and fully asymmetric by $Re = 400$.

Using experimental methods,[21] and[23] noted that a regime change occurs at $Re > 420$, becoming completely random at $Re = 480$. In contrast,[24] utilized direct numerical simulation to analyze the flow over a sphere within the range

$350 < Re < 425$ to establish the regime where planar symmetry is maintained. This study identified that the planar symmetric regime spans $350 < Re < 375$, which contradicts the experimental findings by[21], which indicated a loss of planar symmetry at $Re = 420$.[24] attributed these discrepancies to the challenges experimental flow visualization techniques face in detecting small-scale variations in the azimuthal angle of vortex formation. Furthermore,[25] observed planar symmetry for $Re < 450$ and instantaneous secondary flow separations at $Re = 450$.

Research by[26],[27],[28],[29], and[30] represents early efforts to explore variations of the standard bluff body by modifying the aspect ratio to create spheroids. Although the literature on this specific bluff body is more limited, its relevance extends to practical applications such as particle dynamics and submarine design. For example,[31] conducted simulations on a suboff bare hull model, demonstrating that the vorticity is significantly influenced by the body's angle of inclination. In submarine-related studies,[32] examined the wake asymmetries at a pitch angle of 12 degrees and Reynolds numbers around 10^6, highlighting the impact of these factors on flow characteristics.

Various configurations of ellipsoidal bodies have been explored to understand flow dynamics under different conditions. For instance,[33] investigated ellipsoids with varying aspect ratios at a Reynolds number of $Re = 300$. Similarly,[34] studied a prolate spheroid oriented perpendicular to the inflow, observing an unsteady wake between $Re = 100$ and $Re = 250$. At a much higher Reynolds number of 10^4, the same study found that such an arrangement disrupts the axisymmetry at the front part of the body within the laminar boundary layer.[35] provided experimental visualizations of the flow over a prolate spheroid at various angles of attack. Additionally,[36] employed Large Eddy Simulation to analyze an inclined spheroid with an aspect ratio of 6:1 at $Re = 4.2 \times 10^6$, emphasizing the significance of near-wall numerical treatment and the complex unsteadiness of the flow.[37] examined the impact of varying angles of attack from 10 to 20 degrees on the flow at the same Reynolds number and aspect ratio, finding that numerical predictions of primary and secondary separations closely matched experimental results.[38] experimentally measured the velocity and highlighted the strong dependence of flow separation and vorticity development on Reynolds number and angle of attack. Alongside[39], these studies provide insights into the flow separation characteristics of a spheroid at different angles of attack. Moreover,[40] delves into the study of wake instabilities at various angles of attack and Reynolds numbers between $Re = 100$ and $Re = 3000$.

The study of interactions between multiple bodies, particularly spheres and ellipsoids, features fewer investigations compared to those using cylinders, as highlighted by extensive research on the latter, such as[41],[42], and[43]. Focusing on spheres,[44] and[45] conducted experimental studies on the effects of two spheres facing each other, elucidating the interactions between them. In a tandem arrangement,[3] explored the dynamics between two spheres in an unsteady and periodic regime. Their findings indicated that the wake structures and fluid forces are significantly influenced by the proximity of the second sphere, which experiences a drag reduction even at distances greater than 8D from the front sphere. Moreover,[2] utilized the volume of solid and Lattice Boltzmann method to study the interaction of dual particles at Reynolds numbers of $Re = 50, 100$, and 200. This research revealed varying flow behaviors depending on whether the arrangement was side by side or at different orientation angles. Additional studies by[46] and[47] further investigated the effects of proximity on sphere dynamics. In another numerical study,[48] examined the wake of three tandem elliptic cylinders for Reynolds numbers ranging from 65 to 160, classifying the flow dynamics into five distinct regimes based on variations in Reynolds numbers and L/D ratios.

In this introduction, it is evident that analyzing flow at low Reynolds numbers presents significant challenges from a fluid dynamics perspective. Additionally, when evaluating tandem configurations, the behavior compared to isolated structures can differ markedly. Consequently, the aim of this research is to numerically investigate the influence of interactions between two similar ellipsoids arranged in tandem, a configuration not extensively explored in existing literature. This evaluation will consider Reynolds numbers of 100, 200, 300, and 400 across two distinct tandem scenarios: one in cross flow and the other at an angle of incidence of 45 degrees between the ellipsoids. The distances between the ellipsoids will vary from 1D to 8D, allowing for a comprehensive analysis of their dynamic interactions.

This paper is organized as follows: Section I introduces the problem and reviews relevant previous research. Section II details the problem description, methodology, computational domain, and fluid parameters used in the study. The procedure described is verified and validated in Section III. Following this, new contributions are discussed through the results presented in Section IV. Finally, Section V summarizes the conclusions of this research.

II. METHODOLOGY

A. Problem description

The research is conducted numerically using an ellipsoid as a bluff body in a tandem arrangement. The geometry is placed in two different orientations: one in a prolate position and the other in a prolate position with an angle of attack of 45 degrees to the flow. The ellipsoid's position is determined by its larger length, which is the one across the fluid. Based on an ellipsoid equation, $\frac{x^2}{a^2} + \frac{y^2}{b^2} + \frac{z^2}{c^2} = \frac{1}{4}$, the dimensions of the ellipsoid remain constant throughout this research being $a = c = 1$ and $b = 2$ which is the longer axis for the geometry. A second ellipsoid, similar to the original, is placed in a tandem configuration. In this configuration, the front ellipsoid remains in the same position for all cases, while the rear ellipsoid is moved to different positions from $a = 1$ to $a = 8$.

B. Numerical considerations

1. Numerical tool

The research employs OpenFOAM, a free, C++-based numerical tool that uses the finite volume method to implement fluid dynamic equations and numerical schemes.

2. Governing equations

In this study, low Reynolds numbers are investigated, $Re = 100$, $Re = 200$, $Re = 300$ y $Re = 400$. Therefore, the Navier-Stokes equations for incompressible and viscous flow is used to model laminar flow in a 3D case. These equations include the conservation of mass and momentum.

$$\nabla \cdot \mathbf{v} = 0 \tag{1}$$

$$\frac{\partial(\rho \mathbf{v})}{\partial t} + \nabla(\rho \mathbf{v}\mathbf{v}) = \rho \mathbf{g} - \nabla p + \mu \nabla^2 \mathbf{v} \tag{2}$$

Where:

- p is the pressure.
- ρ is the fluid density.
- μ is the fluid viscosity.
- $\mathbf{v}$ the velocity vector,

More detailed description on the equations and numerical methods can be found in[49],[50] and[51].

3. Numerical method

The PIMPLE algorithm is adopted to simulate transient and incompressible flows. This algorithm combines the PISO (Pressure Implicit with Splitting of Operator) and SIMPLE (Semi-Implicit Method for Pressure-Linked Equations) algorithms. The simulation involves a single fluid and therefore does not use a turbulence model. Backward time discretization and Gauss linear convection schemes are employed in this study.

The numerical domain presented in II C 1 has different boundary conditions which are; zero normal gradient for pressure at inlet with velocity, $\bar{v}$, being the mean. At the outlet boundary condition, zero velocity gradient and outlet wall are used for pressure. The ellipsoid is defined as a rigid wall, so no slip for velocity and zero normal gradient for pressure are employed. As this is a 3D problem, the other boundaries are considered as walls with slip conditions.

C. Dimensionless parameters

In this research, different Reynolds numbers' scenarios are conducted. The time-averaged forces are presented in a dimensionless form using the drag coefficient (C_D) and the lift coefficient (C_L). The lift is only evaluated when the ellipsoid is rotated to assess the proportion of forces in the y direction that are not apparent in the prolate position. The coefficients are defined as follows:

$$C_D = \frac{X_{Force}}{\frac{1}{2}\rho A v^2} \tag{3}$$

$$C_L = \frac{Y_{Force}}{\frac{1}{2}\rho A v^2} \tag{4}$$

A is the area ($A = \pi \cdot a \cdot /4$), ρ is the fluid density, v denotes the mean velocity profile and forces are evaluated based on those obtained from the ellipsoid. The shedding frequency is determined using the Strouhal number (St), which is defined as follows:

$$St = \frac{fD}{v} \tag{5}$$

The shedding frequency, denoted by f, is obtained by analysing the forces data using a Fast Fourier Transform (FFT). For simplicity and comparison with other research, the variable D is adopted instead of a, where $a = b = D$ in terms of dimensions.

1. Numerical domain and mesh

To conduct this research, a computational domain is created and presented in Figure 1. Various sizes are tested to eliminate any numerical influence from the boundaries. The dimensions of the domain are listed in Table I.

TABLE I: The dimensions of computational domain (relative to D)

	D	$H(D)$	$F(D)$	$B(D)$	$A(D)$	$E(D)$	$L(D)$
Domain size	1	5	25	10	5	5	1 to 8

Mesh quality is a crucial aspect of CFD analysis. This subsection describes the mesh structure used in this work. Various meshes are tested to minimize numerical uncertainties. Section III conducts numerical sensitivity analysis using the meshes described here.

The mesh is created using the free tool snappyHexMesh. The process involves using four boxes and a final boundary layer refinement of 12 layers around the ellipsoid. Different meshes are created: firstly, a mesh is created for an isolated

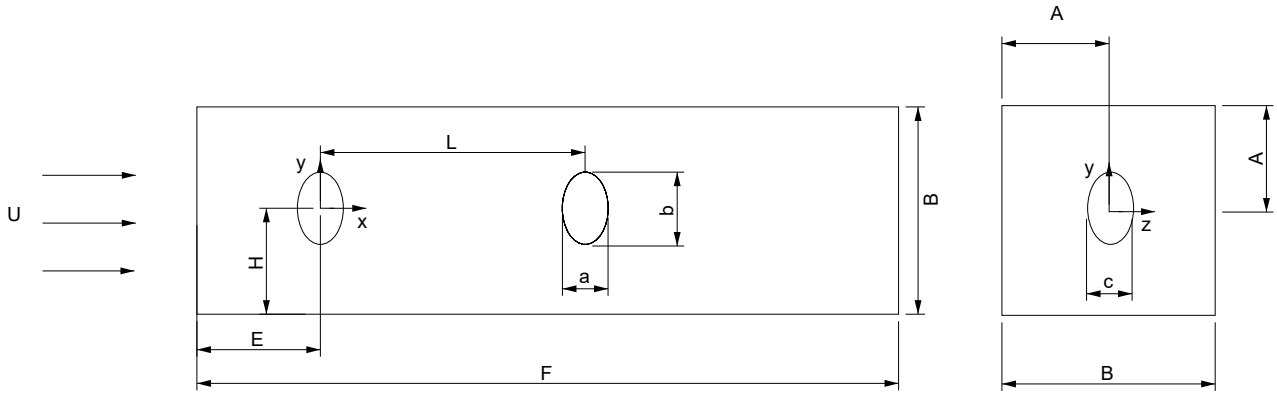

FIG. 1: Computational domain

sphere which will be used for validation purposes. The geometry of this mesh is altered from a sphere to an ellipsoid. After validation, a new mesh is created to match the structure of the previously indicated mesh, but for two objects arranged in tandem. The mesh is presented for a tamdem case in Figure 2a. In Figure 2a the 3D mesh is presented with the two ellipsoids arranged in tandem. In Figure 2b, a closer examination of the mesh in the x-y plane allows for a better understanding of the mesh surrounding the ellipsoid. This is where the boundary layer around the object can be observed. Finally, in Figure 2c a 2D plane view in x-y axes is presented. Here it can be identified the different blocks in which the mesh are subdivided.

The initial block, B1, covers the entire domain with dimensions of 60 in the x direction, 30 in the y direction, and 30 in the z direction. The subsequent boxes halve the number of cells in their respective regions compared to the previous box. Therefore, box 2, named B2, reduces the number of cells in the domain by half compared to B1. Only the region where B2 is located is affected. The procedure for the remaining boxes is identical. Table II presents the coordinates for block three (B3), block four (B4), and B2. These boxes are constructed around an ellipsoid, with their initial coordinate position ($coordinate_{ini}$) and end coordinate position ($coordinate_{end}$) determined accordingly. Additionally, 12 boundary layers are added to the boundary layer treatment. The final mesh presented in Figure 2 will be modified to perform a numerical sensitivity analysis while maintaining its structure.

TABLE II: The detailed coordinates for block two (B2), block three(B3) and block four (B4).

	x_{ini}/D	x_{end}/D	y_{ini}/D	y_{end}/D	z_{ini}/D	z_{end}/D
*B*2	-1.8	3	-1.6	1.6	-2	2
*B*3	-1.3	2.4	-1.2	1.2	-1.5	1.5
*B*4	-1	2	-1	1	-1.2	1.2

Two meshes are created for the validation case based on this mesh structure. The first mesh, called Mesh 1, contains 1,115,537 cells, while the second mesh, called Mesh 2, contains 2,710,549 cells, finally the third mesh called Mesh 3 has 2208378 cells. When considering two spheres, the mesh structure remains the same, but the number of cells increases proportionally due to the domain size increment in the x direction. The mesh used for this work, presented in Figure 2, contains 3,694,436 cells.

III. SENSITIVITY ANALYSIS VALIDATION AND VERIFICATION

This section presents the sensitivity analysis, which is essential for accepting any new results by comparing them with previous literature. The two lines that have been dealt with are mesh and time step verification, along with the numerical procedure. This study evaluates the case of an isolated cylinder at Reynolds number of 300 and compares it with previous research on drag coefficient mean and shedding frequencies through Strouhal number.

Figure 3 shows the drag force over time for a single sphere. The plot demonstrates that the forces converge and oscillate around a certain value. The point at which the signal becomes periodic is the starting point for result extraction and analysis, as previous values are not considered. As shown in Figure 3, this point is reached at approximately 80 seconds.

In Table III, the mean drag forces and Strouhal number are compared with previous research. Different meshes and time steps have been evaluated for the case of a single sphere at $Re = 300$. It is shown that once the mesh reaches a limit of cells, there is no significant change in the drag forces or the shedding frequency. The time step is also verified without the need to use smaller time steps. Therefore, the structure of mesh 1 and the time step $\Delta t = 0.01$ is used for the rest of the proposed research. Finally, these results show that the numerical setup and procedure are valid for this problem since the results are consistent with precious research.

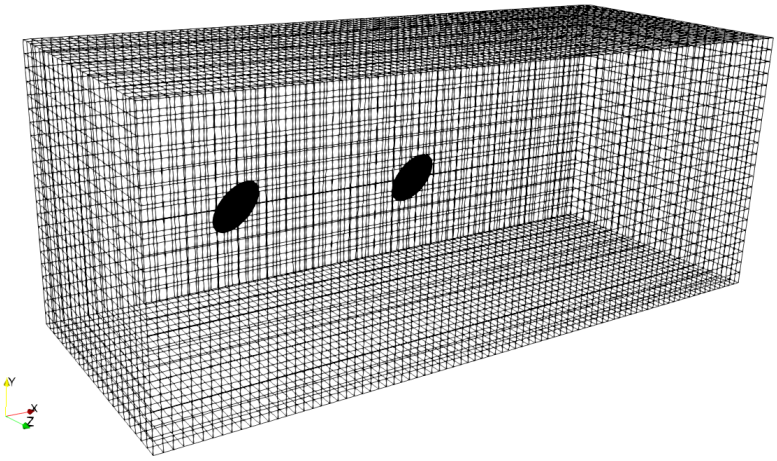

(a) 3D mesh view of the ellipsoids in tandem

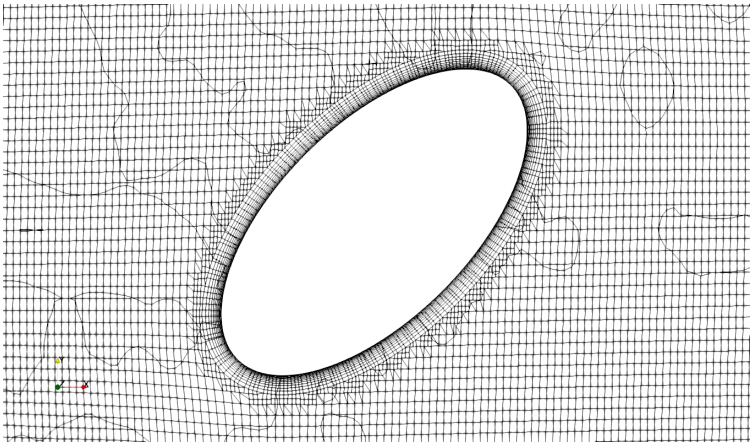

(b) Zoom of the mesh close to the ellipsoid.

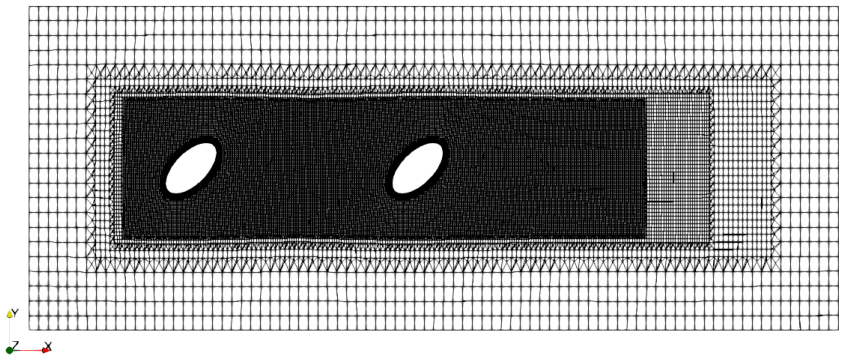

(c) X-Y plane mesh view

FIG. 2: The detailed computational mesh

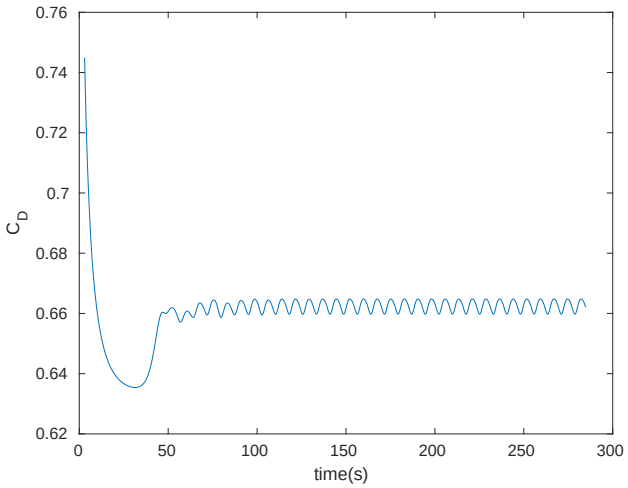

FIG. 3: Drag evolution along simulation time at Re = 300

TABLE III: Sensitivity analysis comparison for flow past a sphere at Re number 300

Case	Δt	C_D	St
52	-	0.65	0.13
33	-	0.66	0.13
20	-	0.66	0.13
Mesh 1	0.015	0.66	0.13
Mesh 1	0.01	0.66	0.13
Mesh 1	0.005	0.66	0.13
Mesh 2	0.015	0.66	0.13
Mesh 2	0.01	0.66	0.13
Mesh 3	0.01	0.66	0.13
Mesh 3	0.0005	0.66	0.13
Mesh 3	0.0001	0.66	0.13

IV. RESULTS

This study investigates the interaction of tandem ellipsoids in two specific orientations: prolate and 45º prolate. The research will focus on a distance up to 8D since the evaluation will focus on the proximity between ellipsoids. The analysis encompasses various Reynolds numbers, beginning at 100—where the flow over a sphere is expected to maintain a steady-state laminar condition—and extending to 300, anticipated to exhibit time-dependent behavior with hairpin vortex formation. Furthermore, the study explores a Reynolds number of 400, where, according to existing literature, the wake is likely to lose planar symmetry. All scenarios are analyzed under laminar flow conditions, with detailed assessments of forces, vortex shedding, and flow visualization.

A. Drag forces analysis

This subsection details the force analysis across different cases, primarily focusing on drag forces. While the primary emphasis is on drag, lift forces will also be examined for the 45-degree prolate case, where, according to previous literature, the forces for the standard prolate configuration are close to zero. Results will be presented in charts that include a baseline comparison against a solitary sphere at the same Reynolds number, sourced from prior studies, serving as a reference point. To clarify the discussion, the following nomenclature is adopted: FE represents the front ellipsoid prolate, while RE represents the rear ellipsoid in prolate. $FE45$ denotes the front ellipsoid 45 degrees prolate, and $RE45$ denotes the rear ellipsoid in 45 degrees prolate.

1. *Re = 100*

Figure 4 shows the comparison of the different C_d for each of the spheroids as the distance between them increases for Reynolds number 100, both for the prolate flow situation and for 45º prolate. First, we see a similar trend in comparison with a sphere arrangement[2]. In general, the maximum difference between the front and rear ellipsoid in both situations occurs for the minimum separation (D) and it decreases as the separation increases. However, for the prolate, a relative minimum between the C_d of both ellipsoids is reached for 3D (Figure 4a), while this reduction is reversed for the 45º position with a relative maximum for 1.5D (Figure 4b). It can also be seen how the effect of the tandem is reduced in the effects on the rear ellipsoid, evidently, as the distance increases, but this effect is much more pronounced in the prolate configuration than in 45º prolate, starting to stabilise from 6D onwards. Likewise, the effect on the front ellipsoid is practically imperceptible in both configurations with variations barely exceeding 0.05 C_d for distances less than 3D and 4D in prolate and 45º prolate, respectively. It can also be observed that, while the maximum C_d for the front ellipsoid is 1 and 0.8 for the front ellipsoid in prolate and prolate 45º, respectively, for the rear ellipsoid it does not exceed 0.6, even for distances of 8D. Figure 4c shows the above, with a difference of 0.2D remaining practically constant between the two arrangements with respect to the front ellipsoid. All this leads us to consider that for values of $Re = 100$ the effect of the rear ellipsoid on the front one is only appreciable at distances smaller than 3D due to the recirculating flow influence between the two geometries, leaving two almost parallel straight lines. Likewise, these small differences in the rear ellipsoid in both configurations are initially maximum, reaching a variation of C_d of 0.1 between prolate and 45º prolate (Figure 4d), but they are rapidly reduced until they become very small from 4D.

2. *Re = 200*

When Reynolds number increases from 100 to 200, the maximum C_d experienced by both ellipsoids decreases by about 20% with respect to $Re = 100$, both at prolate and prolate 45º (Figure 5) as normally occurs with a sphere. While C_d is around zero when the separation is less than 1.5D for the rear ellipsoid in the prolate position (Figure 5a), at 45 pro-

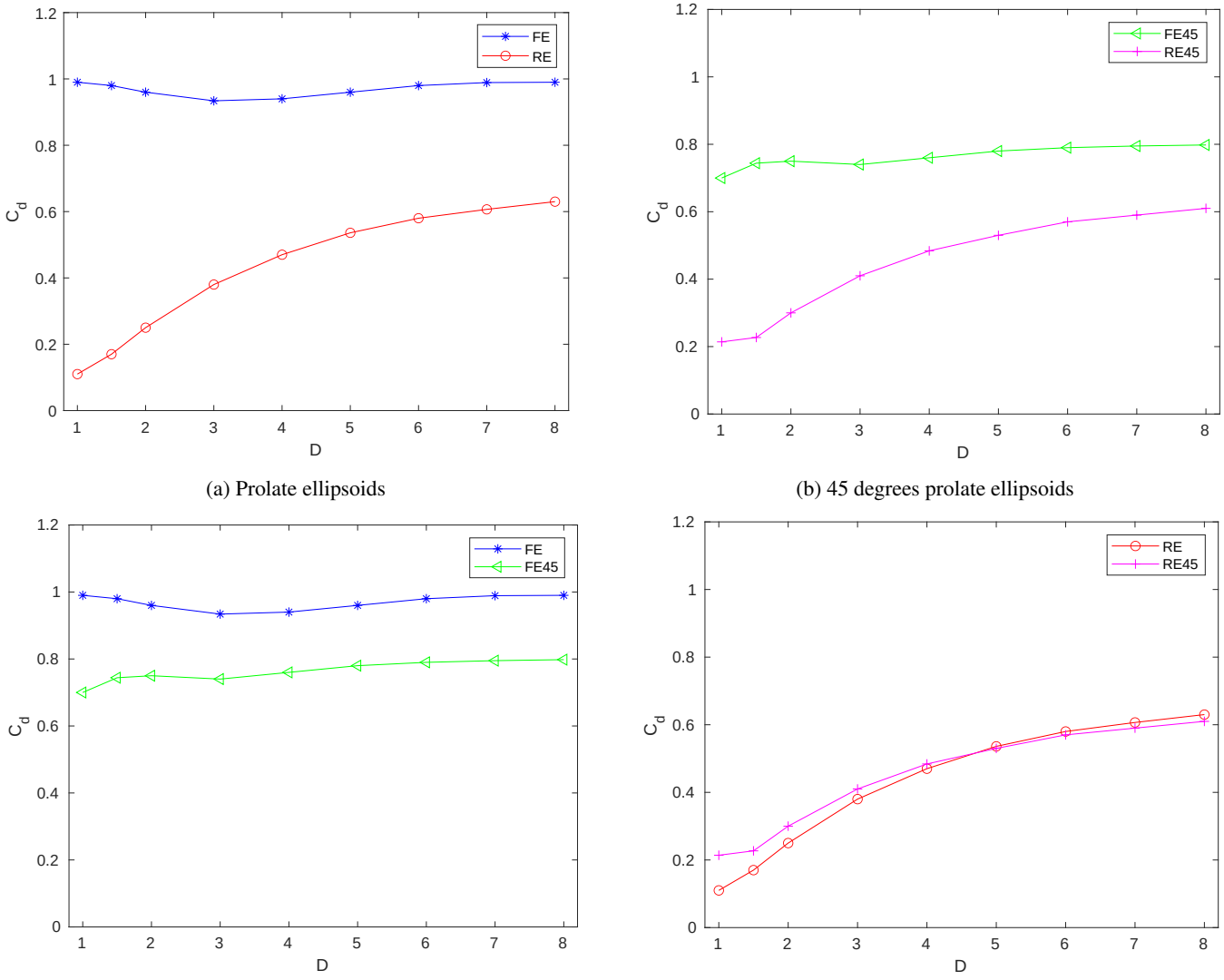

(a) Prolate ellipsoids

(b) 45 degrees prolate ellipsoids

(c) Front ellipsoids

(d) Rear ellipsoids

FIG. 4: Drag force coefficient for tandem ellipsoids and Re = 100

late it starts from a value of 0.1, increasing smoothly to 0.5 for a separation of 8D (Figure 5b). In the case of prolate position, C_d for rear ellipsoid increases much faster than 45 prolate up to a distance between ellipsoids of 5D. From here, it increases slightly to a distance of 6D, decreases noticeably below 0.5 at 7D and finally ends at 0.5 for the maximum ellipsoid distance evaluated. The same behaviour can be seen for the front ellipsoid from 5D onwards, with both forces remaining parallel (front and rear) with a phase difference of approximately 0.25, although at lower distances there is practically no change in C_d, remaining at around 0.75. This phase difference between both ellipsoids is reduced to half for 45 prolate (Figure 5b), also from 6D onwards, although without relative maxima or minima in any of the ellipsoids. Figure 5c shows that C_d remains almost constant on the front ellipsoid within 0.5, as was the case for Re=100 (Figure 4b). However, C_d on the rear ellipsoid for $Re = 200$ (Figure 5d) differs significantly with respect to $Re = 100$ (Figure 4d). While for the latter, the difference between C_d in both positions was negligible, becoming identical from 4D (Figure 4d), for the former (Figure 5d) C_d for prolate position at 45º remains 0.1 above prolate until 3D, where it increases rapidly to 0.1 above prolate at 45º until 6D, decreasing to reach the same value from 7D onwards in the rear ellipsoid for both positions.

3. *Re = 300*

Figure 6 shows the results obtained for Reynolds number 300. In general terms, the behaviours of both ellipsoids are quite similar to those observed for Re=200, although C_d is lower when compared as expected based on the sphere previous literature, except for the rear ellipsoid for prolate which increases slightly from a distance between ellipsoids of 6D.

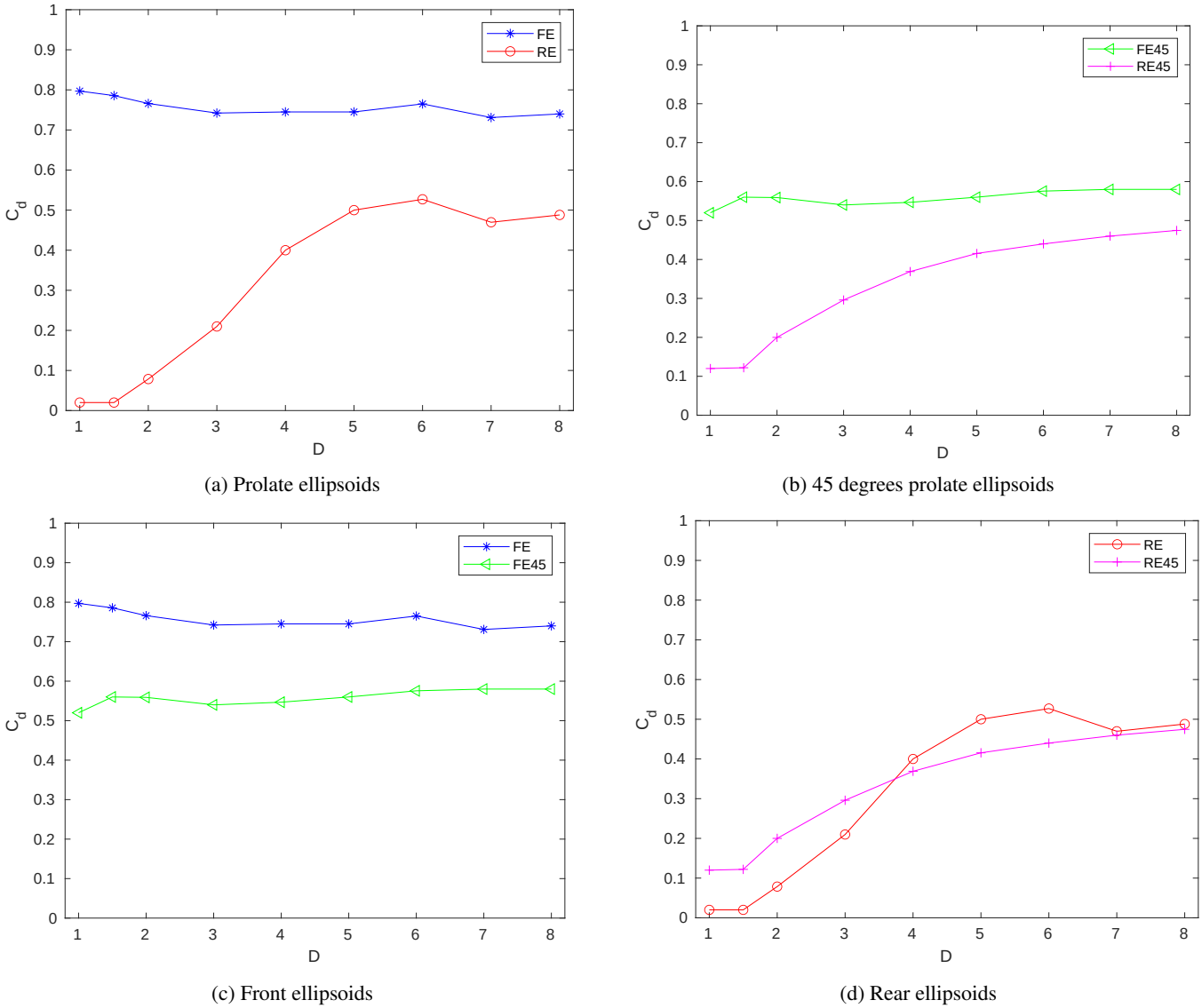

(a) Prolate ellipsoids

(b) 45 degrees prolate ellipsoids

(c) Front ellipsoids

(d) Rear ellipsoids

FIG. 5: Drag force coefficient for tandem ellipsoids and Re = 200

For the front ellipsoid, the separation between the two elements has hardly any effect on C_d except for separations smaller than 1.5D for 45º prolate (Figure 6c), where a slight decrease of 0.5 is noticed. The difference between the C_d values for Re=200 and Re=300 for the front ellipsoid is a decrease of 0.1 in both cases. In the case of the rear ellipsoid for prolate position, the effect of the flow only starts to be perceived at 2D (Figure 6a), a distance somewhat greater than Re=200 (1.5D). From this separation between objects, C_d starts to increase rapidly until an inter-distance of 5D, where it stabilises around 0.55 and 0.45 in prolate and prolate 45º, respectively. However, the rate of increase of C_d is much higher in prolate (0.2/D) than in prolate 45º (0.1/D), being in both cases also more pronounced than for Re=200 (Figure 5). If we compare the rear ellipsoid for both arrangements (Figure 6d), we can see that, as for Re=200, C_d of prolate 45º remains above prolate position until 3D, where the terms are inverted, leaving a constant offset of 0.1 of one over the other from 6D onwards, instead of converging in similar values as was the case for Re=200.

4. *Re = 400*

The resulting differences between the two ellipsoids for Reynolds number 400 (Figure 7) are maximum the closer the objects are, although they become progressively smaller as the separation increases, leaving a difference of 0.05 for the maximum separation (8D). However, this value occurs from 4D onwards, remaining constant for the case of 45º prolate. The non-existence of drag force on the rear ellipsoid, which occurred up to 2D for Re=300 in prolate configuration (Figure 6), is not reproduced for Re=400 as can be seen in Figure 8a, starting from a C_d of 0.05, both in this configuration and 45º

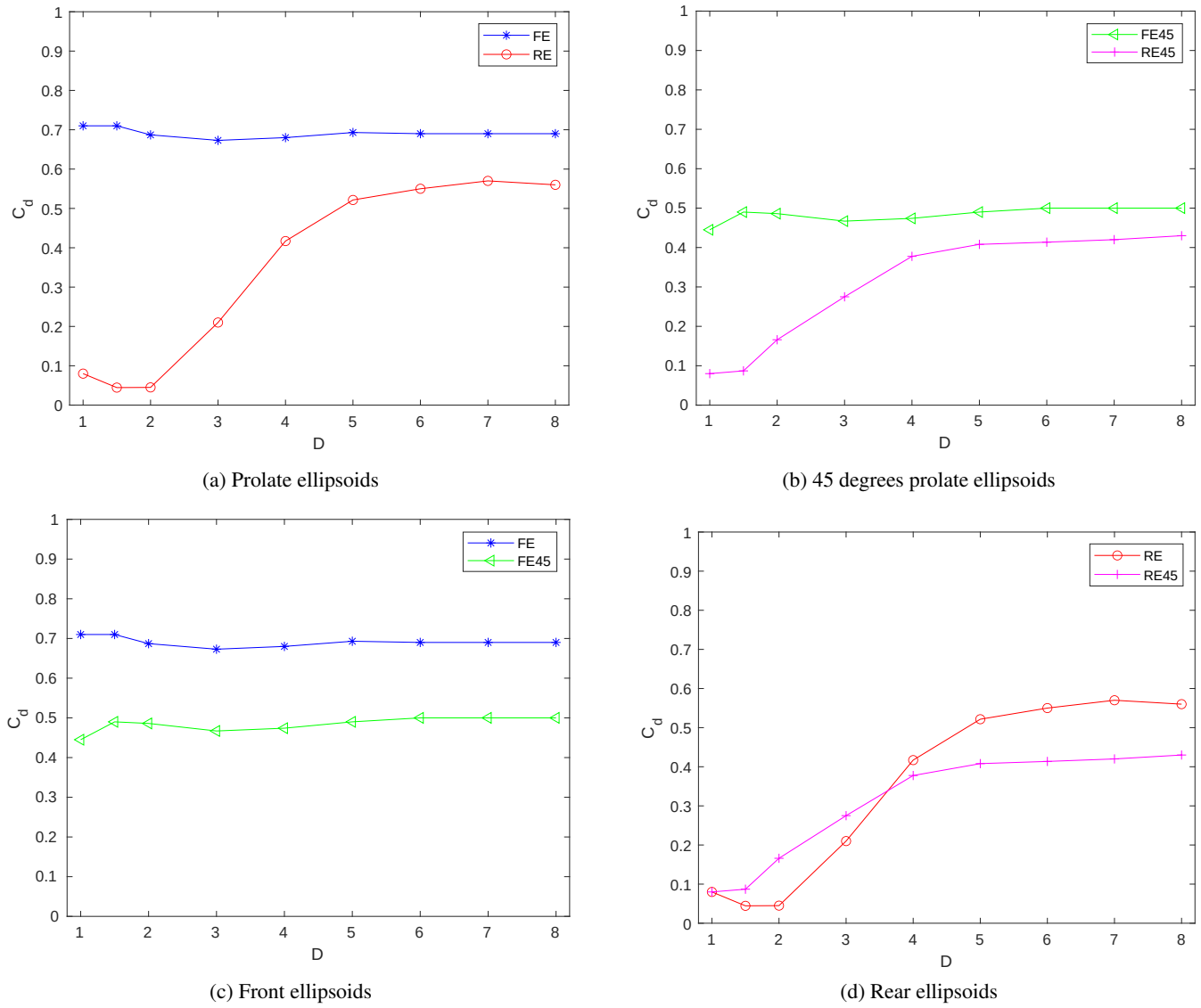

(a) Prolate ellipsoids

(b) 45 degrees prolate ellipsoids

(c) Front ellipsoids

(d) Rear ellipsoids

FIG. 6: Drag force coefficient tandem for ellipsoids and Re = 300

prolate. On the other hand, contrary to the previous cases, C_d does not remain constant for spacings smaller than 3D and prolate in the case of the front ellipsoid (Figure 8b), varying between 0.4 and 0.75, while for 45° this value always remains around 0.45. Regarding the different positions of the rear ellipsoid (Figure 8b), no significant variations are observed in C_d up to a distance of 4D, from which the 45° prolate remains constant at 0.4. On the contrary, in the prolate situation the drag force increases progressively until it reaches 0.6, only 0.05 below the front ellipsoid.

B. Lift forces analysis

This section delineates the analysis of lift forces acting on the y-axis, which are presented in a dimensionless format. These forces have been calculated as the mean values once the results stabilized, a method consistent with the approach taken for drag forces. Notably, lift forces in the prolate case are omitted from this presentation. As established in prior studies, such forces are approximately zero and do not vary significantly. In contrast, the prolate 45 case exhibits distinct behaviour; the rotation of the ellipsoid generates a significant lift force. These forces are illustrated in Figure 8, which displays the forces exerted by the front and rear ellipsoids, on the left and right respectively, across the studied Reynolds numbers.

With regard to the lift forces, the rear ellipsoid consistently exhibits a reduction in force compared to the front ellipsoid, which is situated within the wake of the front sphere. The force trend for the front ellipsoid mirrors that observed in the Reynolds numbers 200, 300, and 400 cases, as depicted in Figure 8a. This trend features a lift force that initially peaks at 2Ds, then diminishes and stabilizes by 3D. Beyond this

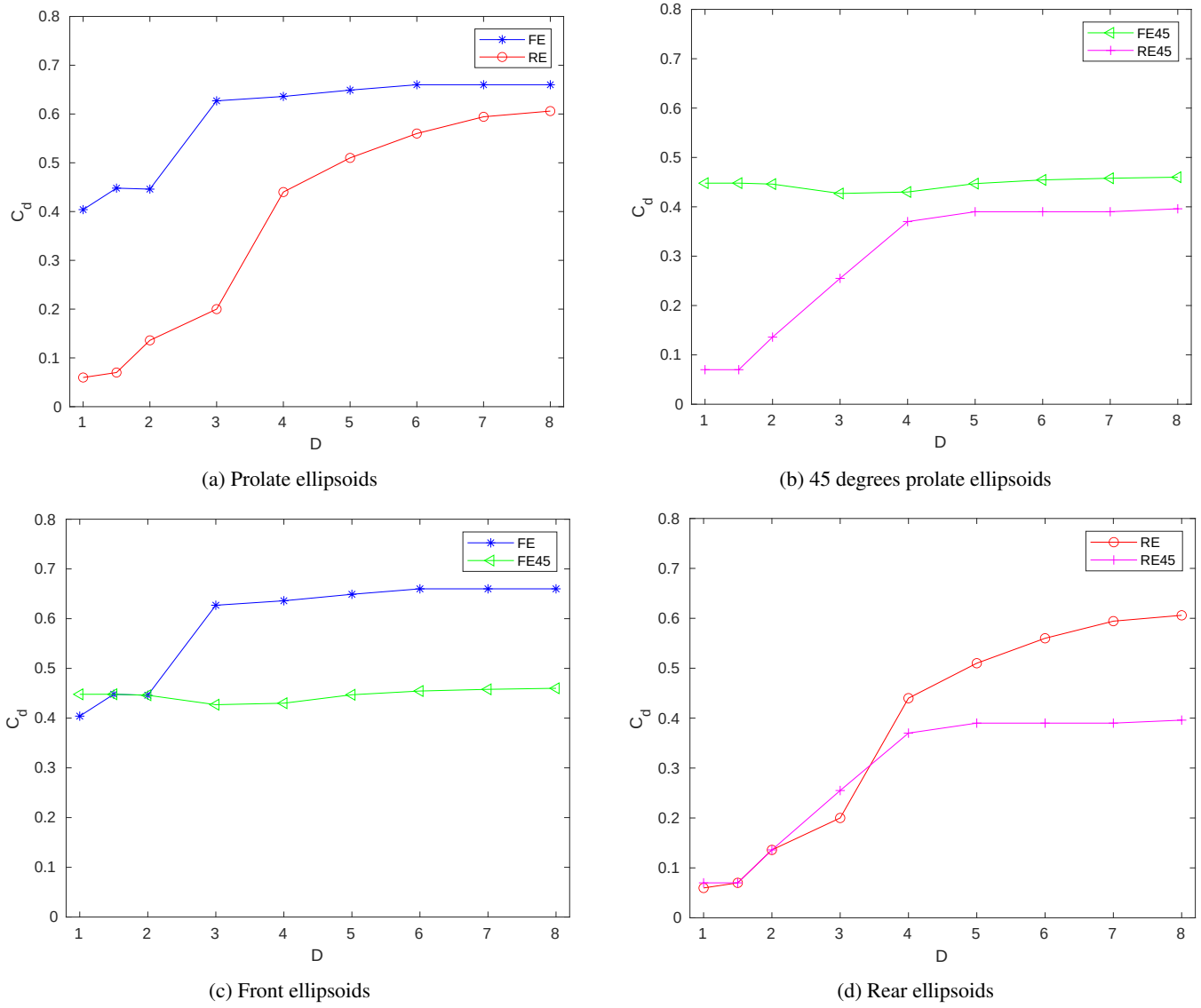

(a) Prolate ellipsoids

(b) 45 degrees prolate ellipsoids

(c) Front ellipsoids

(d) Rear ellipsoids

FIG. 7: Drag force coefficient for tandem ellipsoids and Re = 400

point, the force remains nearly constant across further separation distances. Notably, the peak force observed for the front ellipsoid aligns with a minimum force point for the rear ellipsoid, as shown in Figure 8b. The data shows a decrease in forces from 1D to a minimum at approximately 2D, followed by an increase with a steeper slope between 2D and 4D and a smaller slope from 4D to 8D. It is noteworthy that for Reynolds numbers 100 and 200, the forces display remarkably similar trends and magnitudes. However, unlike the front ellipsoid, the highest forces per distance are noted at higher Reynolds numbers for the rear ellipsoid.

C. Flow analysis

1. *Average velocity flow*

Figure 9 presents the mean velocity contour for two distinct Reynolds numbers, $Re = 100$ and $Re = 300$, across two spacing scenarios, namely 1.5D and 8D, which represent the distances between the ellipsoids. These specific cases are chosen to concisely demonstrate the most pronounced variations observed. An initial examination of the velocity contours reveals a significant disparity in the wake characteristics of the prolate ellipsoids compared to those oriented at a 45° angle. This contrast underscores the influence of ellipsoid orientation on wake behaviour and flow dynamics.

The case of $Re = 100$ and 1.5D illustrates how, when the two ellipsoids are in close proximity, they function as a single body. This is evidenced by the fact that the wake of the first

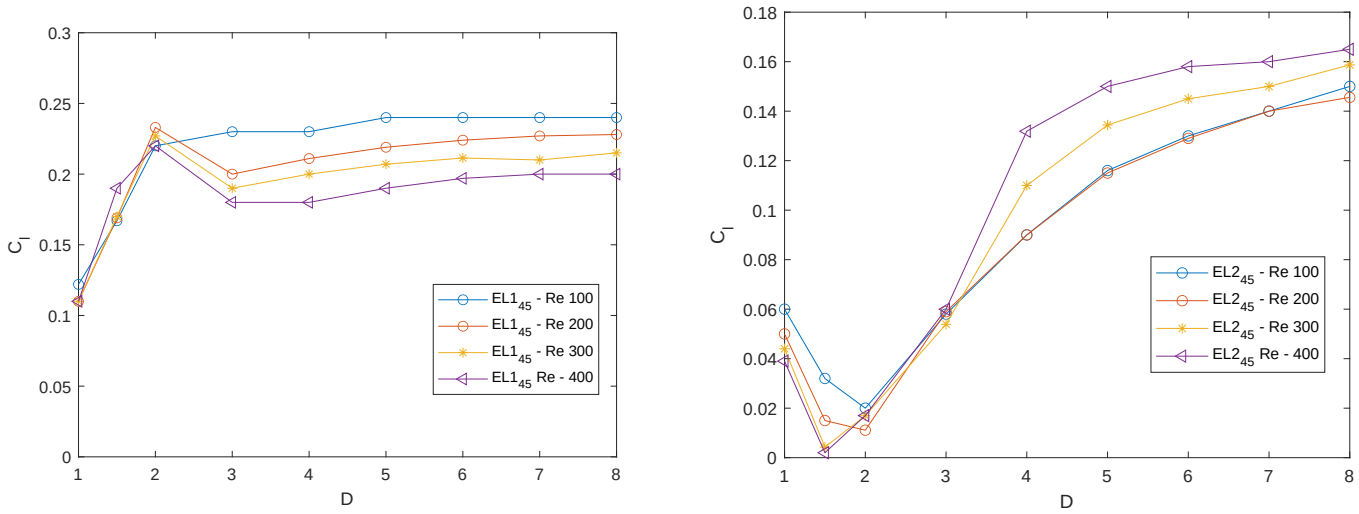

(a) Front 45 prolate ellipsoid

(b) Rear 45 prolate ellipsoid

FIG. 8: Lift force coefficient for tandem ellipsoids

ellipsoid is not fully developed and is joined to that of the second ellipsoid. This phenomenon occurs in both prolate and prolate 45° cases. In the case of prolate 45°, the wake loses its symmetry observed in the case of spheres or cylinders and moves to the upper part of the ellipsoid, which is further away from the flow inlet.

In the Reynolds number of 100 and 8D case, the wake generated by the frontal ellipsoid in the prolate configuration extends until it reaches the sonication point of wake two, where it joins. This illustrates that even at this distance, the front ellipsoid exerts a significant influence on the flow input of the rear ellipsoid. This is evident in the forces presented, as the drag forces of both ellipsoids do not merge, resulting in high variations between them. In the case of prolate 45, there is a notable difference, whereby the wake of the front ellipsoid exhibits a smaller recirculation area. As illustrated by the velocity contour, the flow that reaches the rear ellipsoid arrives with a higher velocity than in the prolate case.

The Reynolds number of 300 case, previously outlined, introduces distinct flow considerations. In the 1.5D scenario, the bodies behave similarly to the Re 100 case, effectively functioning as a single body. However, in the prolate orientation, there is an observable increase in flow velocity at the top and bottom of the rear ellipsoid. This phenomenon is attributed to the increase of Reynolds number, which also alters the inflow and subsequent flow detachment. As the distance between the spheres extends, a suction zone develops, potentially reducing the drag on the front ellipsoid for distances ranging from 1.5D to 5D, as indicated by the measured drag forces. Notably, the zones of increased velocity near the second ellipsoid are exclusively observed in the 45° case, particularly in the lower part of the rear ellipsoid (the attack zone of the ellipsoid).

As the distance between the two ellipsoids increases to 8D, it becomes evident that the prolate trails for both the front and rear ellipsoids are symmetric. The recirculation zones present different areas and different sizes, which are set to be analyzed in more detail later using surface LIC techniques. In the scenario of the 45° prolate, the recirculation zone is significantly smaller. The introduction of an angle of inclination to the ellipsoid enables the front ellipsoid to exert a reduced influence on the rear ellipsoid at a much shorter distance, as evidenced by the velocity contours.

2. *Surface LIC contours*

This section is expanded using the Line Integral Convolution (LIC) technique, a method for visualizing vector fields. This approach can provide additional insights into the recirculation of the flow passing two tandem ellipsoids for the prolate and prolate 45º cases.

Figure 10 and 11 depicts a cut on the z=0 axis, which presents the LIC surface for the mean velocity field. The selected cases are 4D and 6D, representing the different Reynolds numbers of this work. The rationale behind selecting these distances is discussed below. It is based on the fact that they are two distances between ellipsoids where the recirculation zone left by the front ellipsoid affects the rear zone in a completely different way.

On the one hand, in Figure 10, the recirculation zone corresponding to the prolate cases is in direct contact with the rear ellipsoid for the Reynolds 100 and 200 cases. Following this Reynolds number, the recirculation zone does not come into direct contact with the rear ellipsoid. However, there is a zone where the wake is stretched between the recirculation zone and the rear ellipsoid. This suggests the presence of a low-velocity zone that extends and connects the wake of the first ellipsoid with the second ellipsoid. In the case of prolate ellipsoids, it can be observed that the recirculation zone is symmetrical in both the front and rear ellipsoids. It is notable that the recirculation zone for different Reynolds numbers in the rear ellipsoid is considerably smaller on the x-axis than the

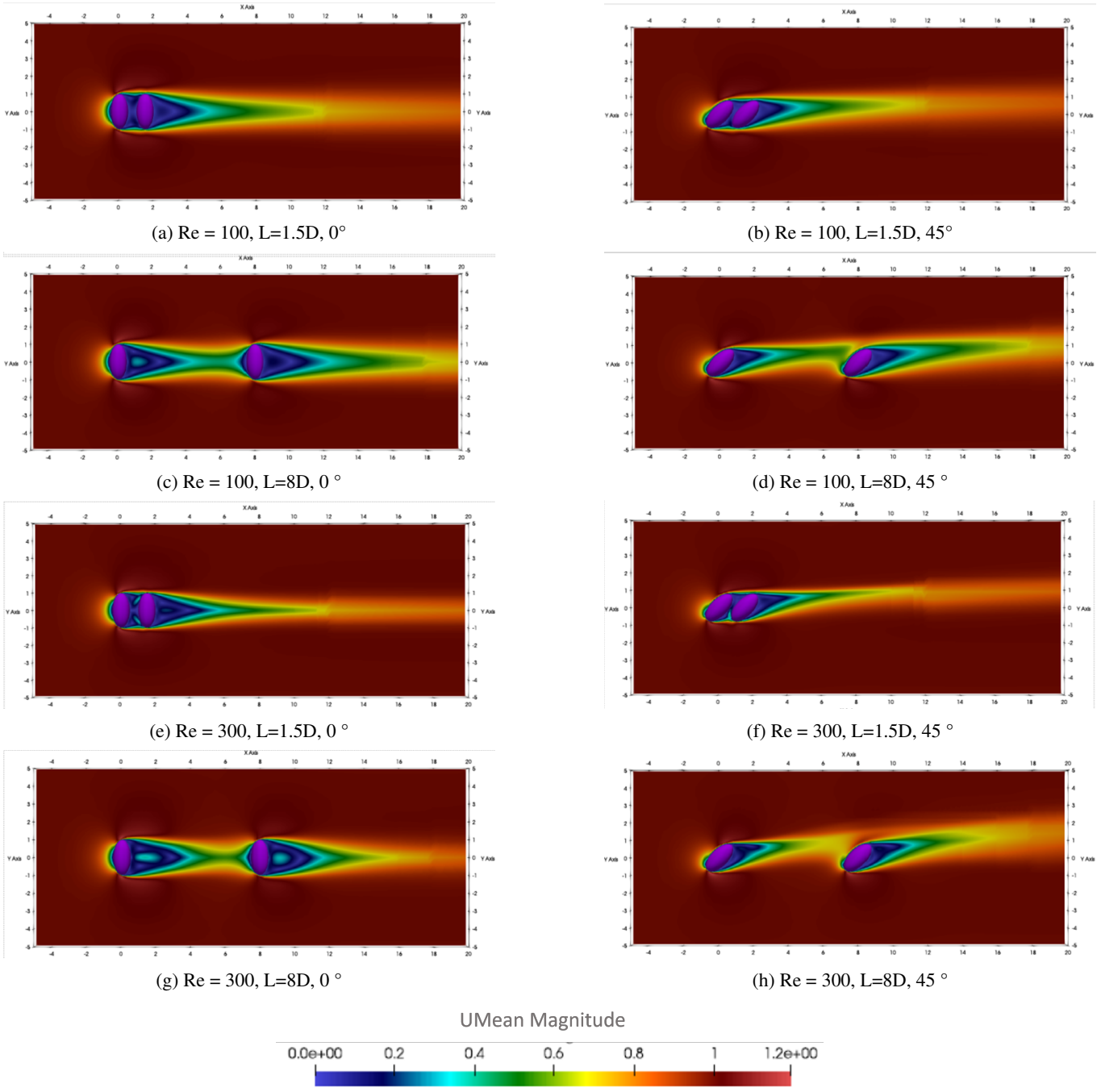

(a) Re = 100, L=1.5D, 0°

(b) Re = 100, L=1.5D, 45°

(c) Re = 100, L=8D, 0 °

(d) Re = 100, L=8D, 45 °

(e) Re = 300, L=1.5D, 0 °

(f) Re = 300, L=1.5D, 45 °

(g) Re = 300, L=8D, 0 °

(h) Re = 300, L=8D, 45 °

FIG. 9: Average velocity field for Re = 100 and 300, 0º prolate and 45º prolate with distance between spheres of 1.5D and 8D

zone created by the front ellipsoid. This is due to the fact that the flow reaching it has a much lower velocity. In general, the size of the recirculation zone in the rear sphere remains relatively constant when the Reynolds numbers change.

Upon analysis of Figure 10, it becomes evident that the fluid dynamics behind the ellipsoids undergo a significant transformation in the context of prolate 45º cases. The symmetry of the wakes behind the ellipsoids is no longer preserved due to the angle of inclination of the geometries. For Reynolds numbers of 100 and 200, it can be observed that in the front ellipsoid, there is a single bubble identified with the recirculation zone. In these cases, the wake that produces velocities close to 0, which in the prolate case came into contact with the rear ellipsoid for this inclination, ends before coming into contact with the rear ellipsoid. Consequently, there is a zone of upward flow through the rear ellipsoid. This suggests that the drag forces of the front and rear ellipsoids for the prolate 45 case at 4D are closer to those of the front ellipsoid due to the wake effect being less pronounced given the inclination and loss of symmetry. Upon increasing the Reynolds number to

300 and 400, it becomes evident that the wake zone left by the frontal ellipsoid is characterised by the presence of two recirculation zones or bubbles. The larger of the two is observed to occupy a central and lower area of the ellipsoid, while the smaller upper bubble is found in the upper area.

A detailed examination of the case of the distance between 6D ellipsoids, as illustrated in Figure 10, reveals that prolate cases maintain symmetry in the wake produced in both the front and rear ellipsoids. This symmetry is lost for the 45 cases. In the case of prolate ellipsoids, the wake and recirculation zone created by the front ellipsoid is stretched until it comes into contact with the rear ellipsoid for Reynolds numbers 100 and 200. This phenomenon is less apparent than when the distance between the ellipsoids is 4D. For Reynolds numbers 300 and 400, a well-defined recirculation zone is observed in the wake of the front ellipsoid, which does not extend to the rear ellipsoid and therefore no longer comes into contact. Nevertheless, the influence of this zone on the wake persists, as the rear ellipsoid receives a considerably lower flux than the front ellipsoid.

In the prolate 45º cases, it is observed that the recirculation zones left by the front ellipsoid are considerably smaller than those observed in the prolate case. It is notable that the rear ellipsoid maintains a recirculation bubble or two for the Reynolds 300 and 400 cases, which are well-defined and become similar to the one produced by the front ellipsoid. This is due to the fact that, at these distances, the wake left by the front ellipsoid affects the rear ellipsoid to a lesser extent.

Figure 12 presents the LIC surfaces for a Y = 0 plane slice, illustrating the XZ flow for the prolate and prolate 45 cases. This cross-section allows us to observe the wake for the Reynolds 300 case and the separation between 5D, 6D and 8D ellipsoids, for the sake of brevity.

This figure illustrates the symmetry observed in the recirculation wake of the prolate case, with both the front and rear ellipsoids exhibiting similar patterns. It can be observed that the recirculation zone of the front ellipsoid is wider and does not connect with the rear ellipsoid. This recirculation zone is even larger on the z-axis than the diameter of the ellipsoid. In the prolate 45º case, the presence of a symmetric recirculation zone in the front ellipsoid is observed. In contrast, the rear ellipsoid exhibits no recirculation bubbles. As illustrated, these bubbles emerge from 6D and become increasingly defined at larger distances, such as 8D.

3. *Flow separation*

Figures 13 and 14 show the instantaneous surface LIC over the surface of the prolate and 45 prolate ellipsoid, respectively, for 2D, 4D and 8D distances and Re 100, 300 and 400. As expected, in the case of the front ellipsoid, the streamlines parallel to the x-axis (Z1) are not altered by the rear ellipsoid and remain at a constant x-width, independent of the separation between them, both the prolate position and the 45 prolate position (Fig 13). As Reynolds number increases, the width of the horizontal streamlines decreases in the Z1 zone and increases in the Z2 zone, where the interaction produced by the rear vorticity increasingly affects the behaviour of the streamlines, and, as a consequence, the earliest detachment occurs.

In the case of the prolate position, the streamlines in the Z2 zone of the front ellipsoid indicate the symmetry of the vorticity and wake along the entire domain, whatever the distance between ellipsoids. In general, three zones can be distinguished in the rear ellipsoid (Z3, Z4. Z5), the intermediate one (Z4) the one that keeps the streamlines parallel to the x-axis, like the Z1 of the front ellipsoid that is affected by the recirculation zone and wake of the front ellipsoid. Z4 is affected by the vorticity and/or wake of the front ellipsoid (Z3) and the last one (Z5) reflects the vorticity created at the back of the rear ellipsoid. The greater the distance between the ellipsoids, the wider the Z4 zone becomes, and the smaller the other two zones become, especially the Z3 zone, reducing the effect of the front ellipsoid on the rear. The extreme case occurs for the separation of 8D and $Re > 200$ when the Z3 zone disappears and the Z4 zone occupies more than 80% of the rear ellipsoid. As Reynolds number increases, the horizontal streamlines, which were clearly delimited by two vertical planes in the rear ellipsoid for Re = 200, start to be affected by the vorticity of the front ellipsoid, especially for 2D where the effect of the front ellipsoid together with that produced at the back of the rear ellipsoid overlap their influence deforming the initial vertical planes (Fig. 13). Likewise, the horizontal streamlines in Z4 are slightly inclined towards the x=0 plane the greater the distance between ellipsoids and the Re.

In the case of prolate at 45º, the symmetry of the previous case is obviously lost, although two (Z1 and Z2) and three (Z3, Z4 and Z5) zones are still differentiated in the front and rear ellipsoids, respectively. The vertical plane differentiating zones in the prolate case becomes a plane that forms an angle of approximately 65º with the x-axis which moves in the opposite direction to the flow (reducing its x-coordinate) as Re increases. As in the previous case, for Re = 200 there is no alteration of the streamlines prior to detachment whatever the distance, remaining horizontal up to the plane dividing zones Z1 and Z2. However, from the detachment plane onwards, it can be assumed that vorticity develops differently as Re increases and may even lead to the formation of double bubbles. As for the prolate position (Fig 14), the detachment for the rear ellipsoid occurred in clearly defined planes except for a distance of 2D, where the Z4 zone is not defined by a plane, but by a curve, as shown in Figure 14. Furthermore, whenever Re > 200, there is a superposition of the vorticity occurring in front of and behind the rear ellipsoid, which causes a continuity of Z3 and Z5 zones and uniformity in the curvature of the streamlines, even with the Z4 zone disappearing for 2D distances, especially in the upper third of the ellipsoid. For Re = 300 it can also be seen that there is a reduction of Z4 in favour of Z3, adapting a distribution of the streamlines along the rear ellipsoid more and more similar to the front ellipsoid as the distance between them increases. Indeed, for Re400 and 8D spacing, the Z4 zone has practically disappeared and the Z3 Zone, with a virtually horizontal distribution of streamlines, occupies about 70% of the rear ellipsoid.

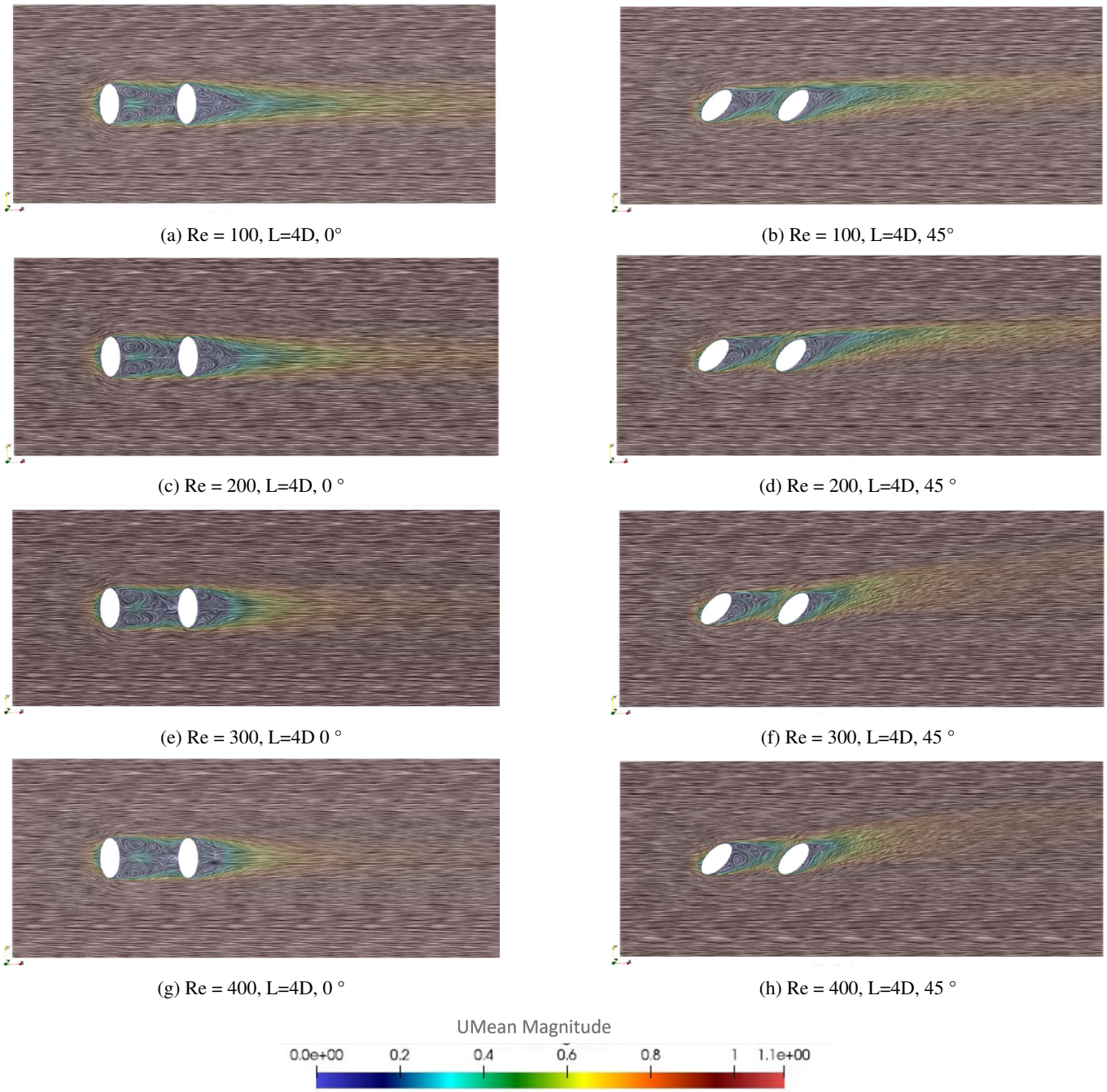

(a) Re = 100, L=4D, 0°

(b) Re = 100, L=4D, 45°

(c) Re = 200, L=4D, 0 °

(d) Re = 200, L=4D, 45 °

(e) Re = 300, L=4D 0 °

(f) Re = 300, L=4D, 45 °

(g) Re = 400, L=4D, 0 °

(h) Re = 400, L=4D, 45 °

FIG. 10: Surface LIC for Re 100, 200, 300 and 400 with distance between spheres L=4D

D. Iso surfaces

Figure 15 illustrates the second invariant of the velocity gradient tensor, computed by the function object for Re = 300 and two separations between ellipsoids, 1.5D and 8D for a plane XY. These instantaneous contours demonstrate the differences that may be observed depending on the orientation of the ellipsoid and the distance between them. In the prolate 45º case, there is a tendency for the iso-surface to ascend, as indicated by the angle of the ellipsoid. Furthermore, the harpein vortex exhibits a markedly more regular structure than in the prolate case. In the 1.5 case, where Q=0.001, the iso-surface structure undergoes a complete transformation, akin to that observed in the sphere case. Those results are also compared with previous research's on sphere[53] and the comparisons show a similar tend.

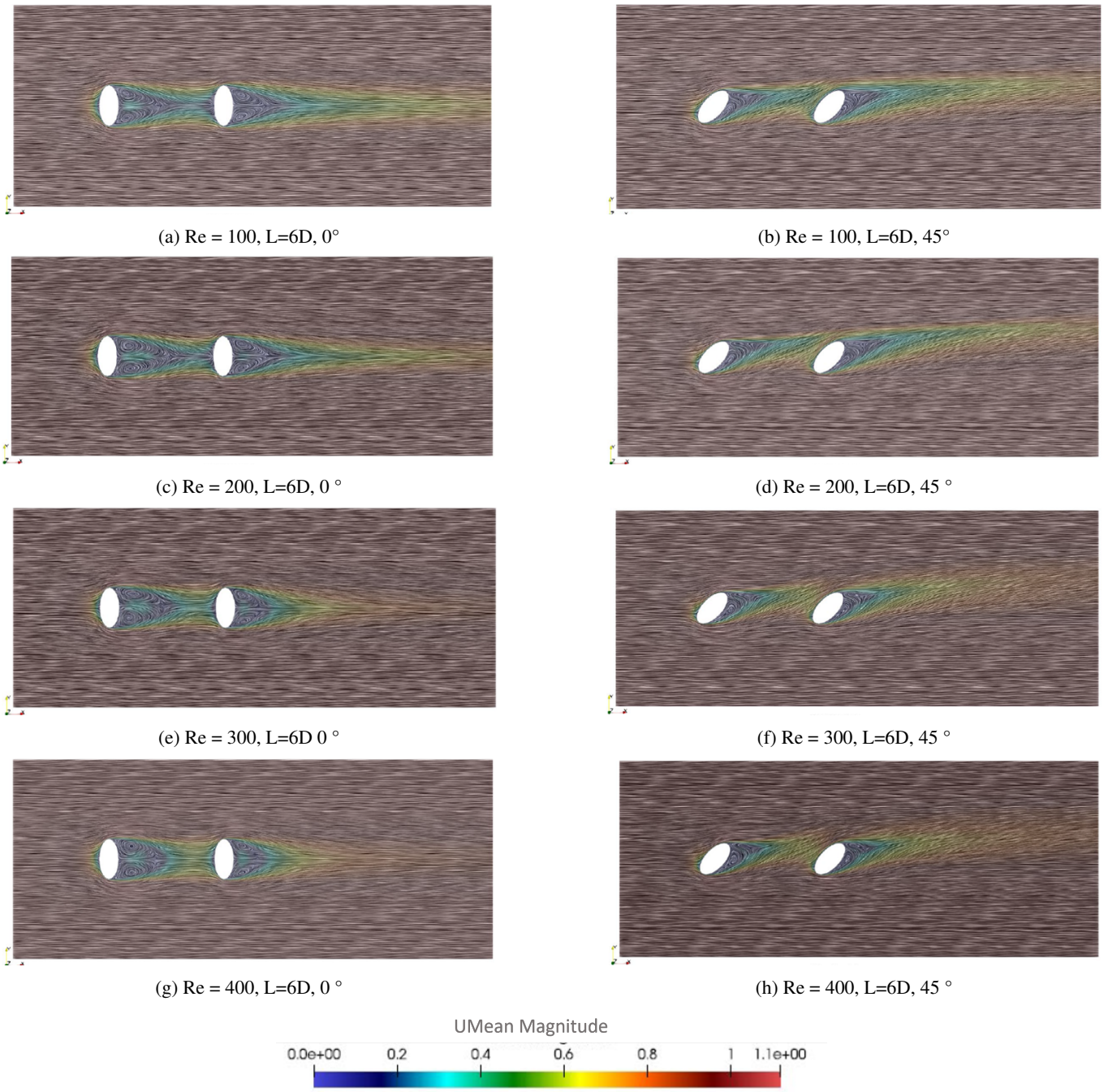

(a) Re = 100, L=6D, 0°

(b) Re = 100, L=6D, 45°

(c) Re = 200, L=6D, 0 °

(d) Re = 200, L=6D, 45 °

(e) Re = 300, L=6D 0 °

(f) Re = 300, L=6D, 45 °

(g) Re = 400, L=6D, 0 °

(h) Re = 400, L=6D, 45 °

FIG. 11: Surface LIC for Re 100, 200, 300 and 400 with distance between spheres L=6D

V. CONCLUSION

This study employs numerical analysis using the open source software OpenFOAM to investigate the hydrodynamic influence of two distinct tandem configurations of ellipsoids, positioned on one side in the prolate position and on the other side in the prolate 45 position, which refers to an angle on the ellipsoid. This was conducted for varying numbers of Reynolds (100, 200, 300 and 400), selected to observe the impact of a steady axisymmetric flow on a steady planar-symmetric regime.

The results indicate that the drag forces tend to equalise or become closer for the prolate 45 cases than in the prolate cases. For Reynolds number 100, the forces acting on the rear ellipsoid are equalised, whereas this is not the case for the other Reynolds numbers. In general, for the prolate cases, there is a distance between 3D and 5D in which the recirculation affects the rear ellipsoid. This is not present in the prolate 45 cases, which would only see the wake of the front ellipsoid, and to a much smaller extent than in the prolate cases.

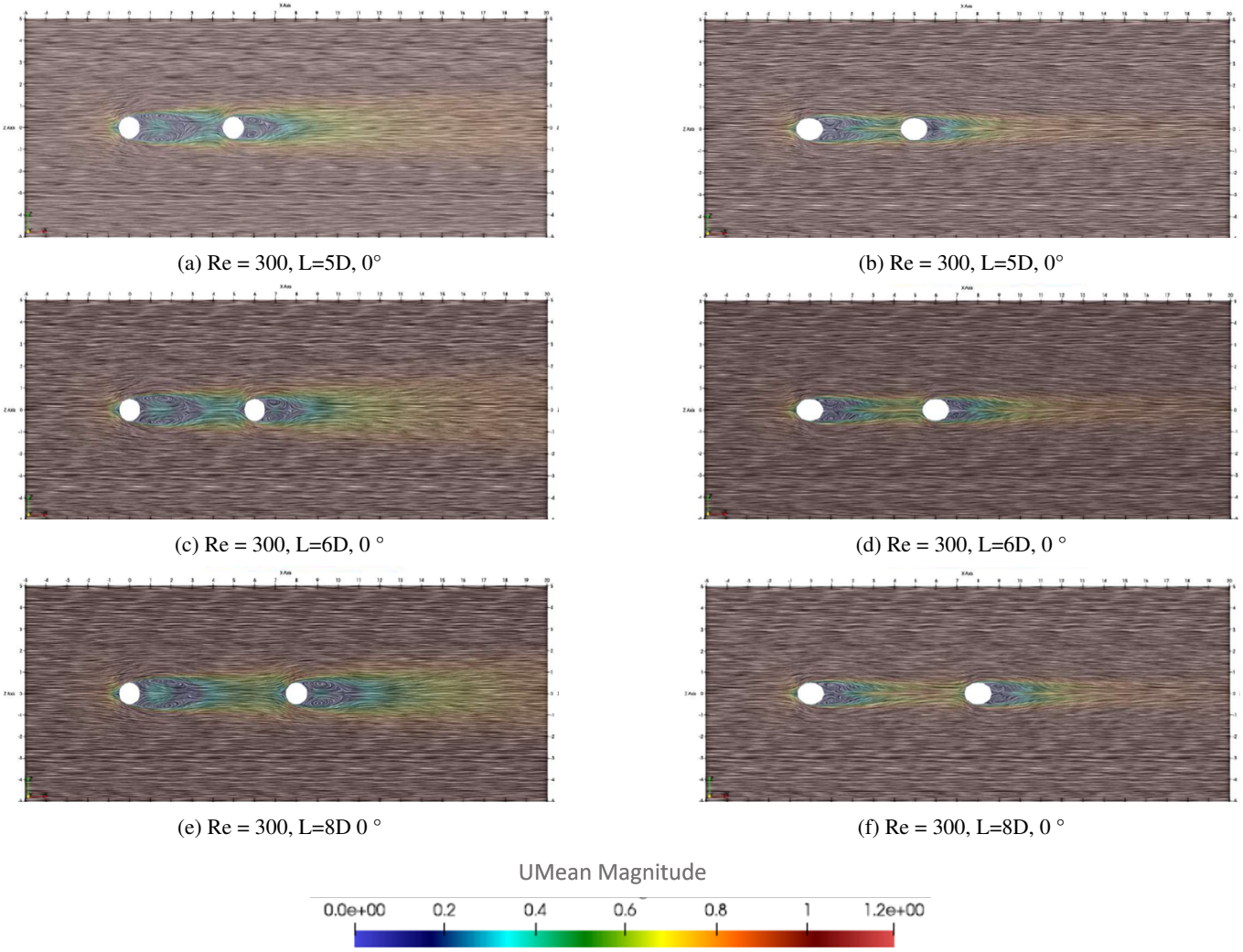

(a) Re = 300, L=5D, 0°

(b) Re = 300, L=5D, 0°

(c) Re = 300, L=6D, 0 °

(d) Re = 300, L=6D, 0 °

(e) Re = 300, L=8D 0 °

(f) Re = 300, L=8D, 0 °

FIG. 12: Surface LIC for Re=300 with distance between spheres L=5D, L=6D and L=8D

The wakes and recirculations between prolate and prolate 45 change completely. The symmetry generated downstream by the flow recirculation is broken when we see an x-y plane. Furthermore, the sizes or areas where recirculation occurs are considerably smaller compared to the same case but with prolate orientation.

Finally, for the lift forces measured in the prolate cases, we observe an opposite tendency of the front ellipsoid versus the rear ellipsoid. While the front ellipsoid exhibits a higher Reynolds number, the rear ellipsoid exhibits a lower lift force. In contrast, the opposite is true. For these cases, we observe a critical point on the two-dimensional plane where, in the case of the front ellipsoid, the forces stabilise, and in the case of the rear ellipsoid, the force undergoes a change in trend, initiating an increasing trend.

DECLARATION OF COMPETING INTEREST

The authors declare that they have no known competing financial interests or personal relationships that could have appeared to influence the work reported in this paper.

ACKNOWLEDGEMENT

The authors acknowledge the use of the IRIDIS High Performance Computing Facility, and associated support services at the University of Southampton, in the completion of this work. H.R. Díaz-Ojeda acknowledges the funding provided by the Ministerio de Ciencia e Innovación through grant PID2022-140481OB-I00.

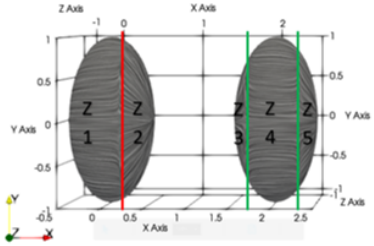

(a) Re = 100, L=2D

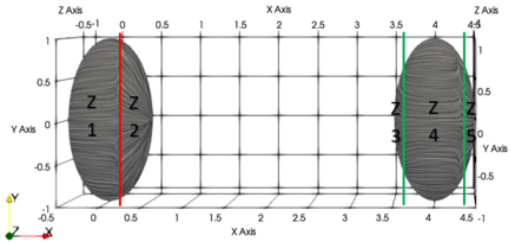

(b) Re = 100, L=4D

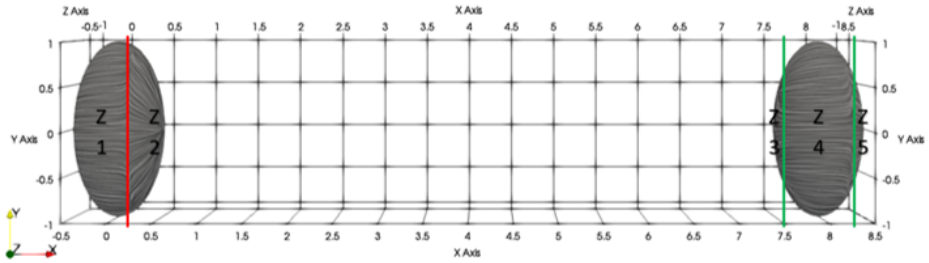

(c) Re = 100, L=8D

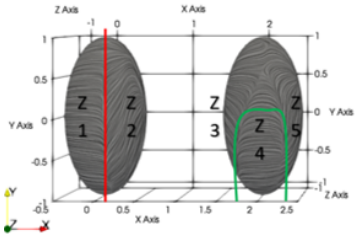

(d) Re = 300, L=2D

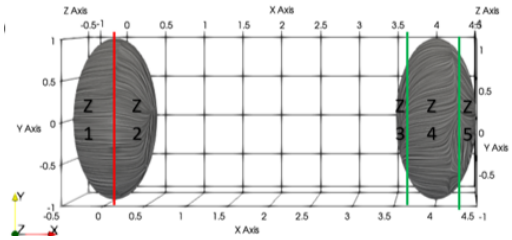

(e) Re = 300, L=4D

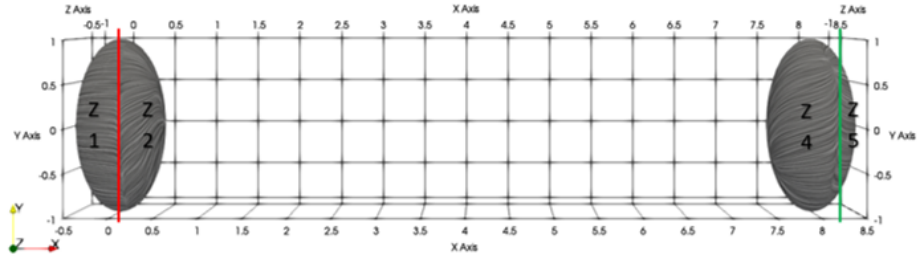

(f) Re = 300, L=8D

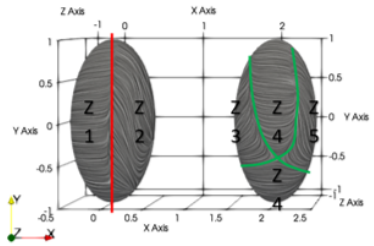

(g) Re = 400, L=2D

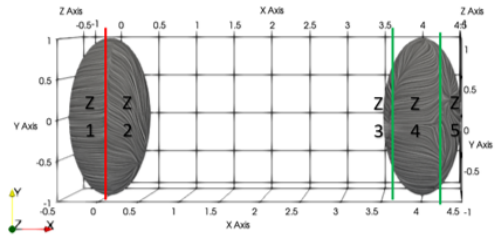

(h) Re = 400, L=4D

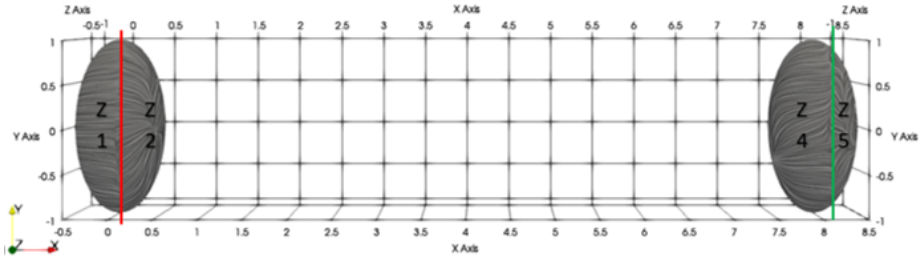

(i) Re = 400, L=8D

FIG. 13: Surface LIC over ellipsoids Re 100, 300 and 400 for 2D, 4D and 8D.

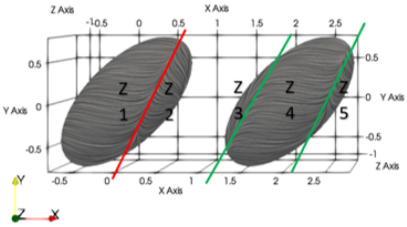

(a) Re = 100, L=2D

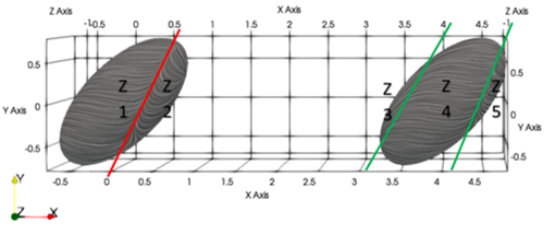

(b) Re = 100, L=4D

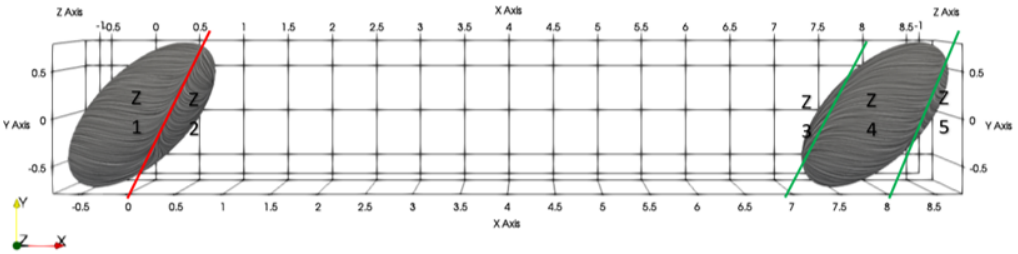

(c) Re = 100, L=8D

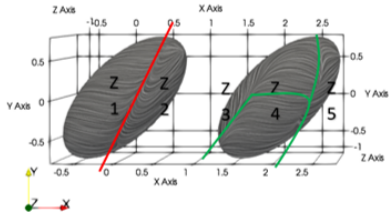

(d) Re = 300, L=2D

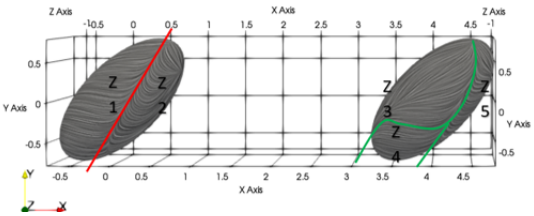

(e) Re = 300, L=4D

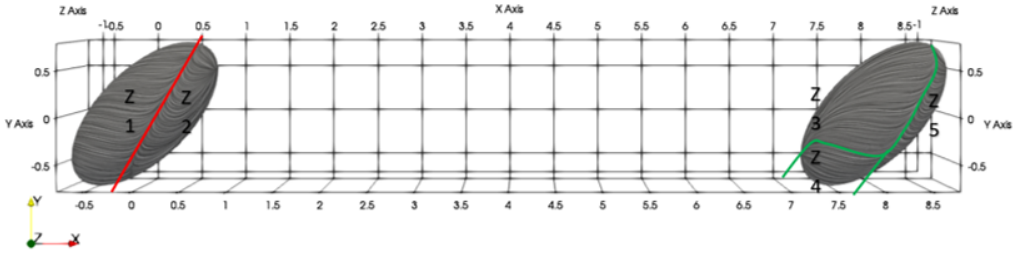

(f) Re = 300, L=8D

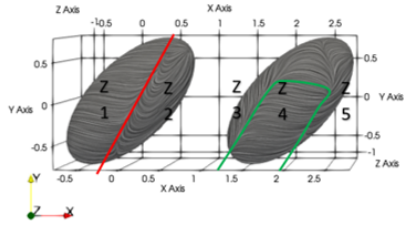

(g) Re = 400, L=2D

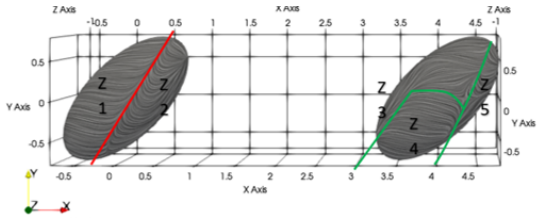

(h) Re = 400, L=4D

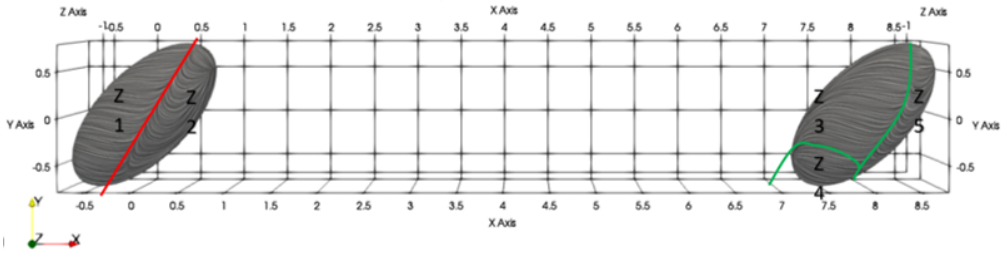

(i) Re = 400, L=8D

FIG. 14: Surface LIC for prolate 45 ellipsoids Re 100, 300 and 400 for 2D, 4D and 8D.

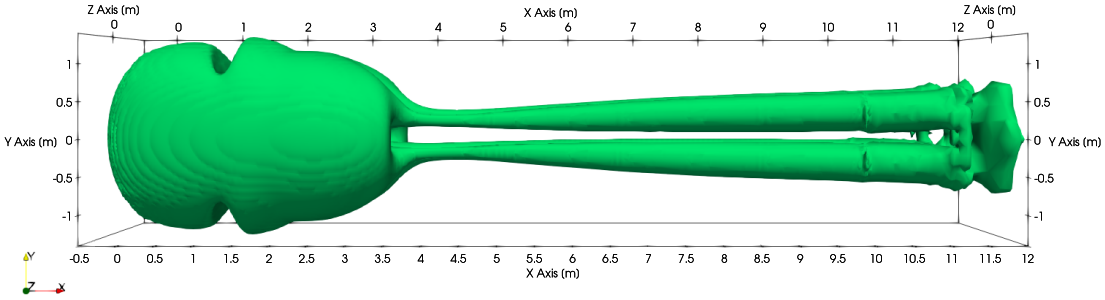

(a) Re = 300, 1.5D prolate

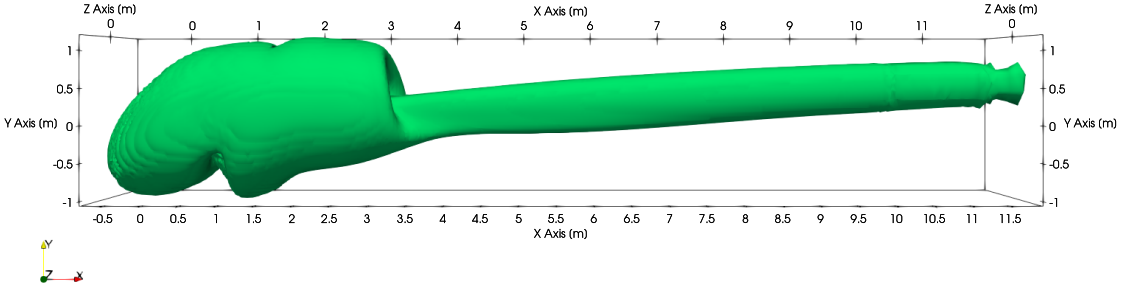

(b) Re = 300, 1.5D prolate 45

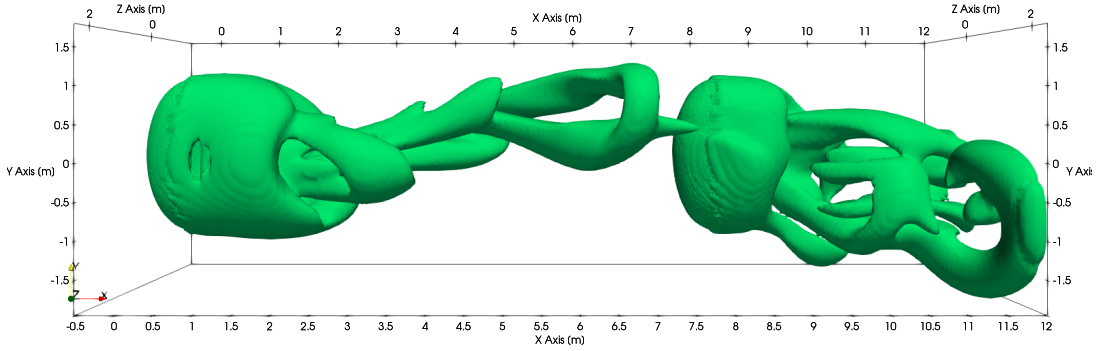

(c) Re = 300, 8D prolate

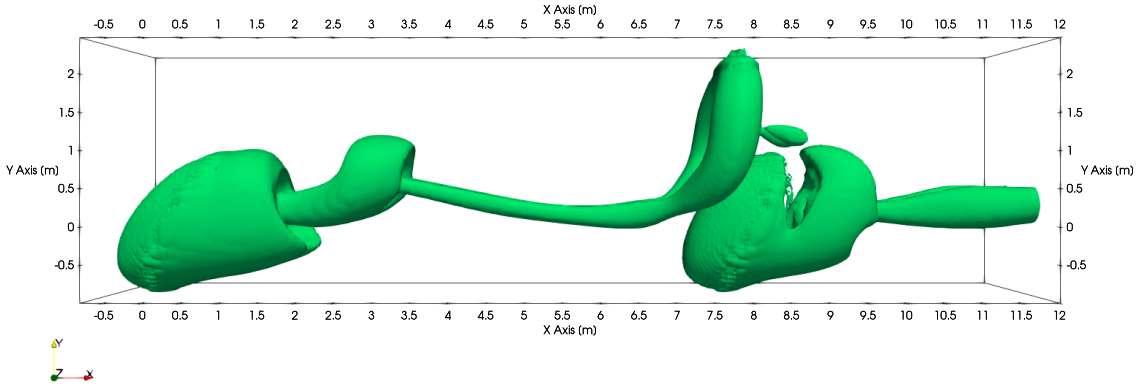

(d) Re = 300, 8D prolate 45

FIG. 15: Q factor for Reynolds number 300 and 1.5D and 8D sphere separation

DATA AVAILABILITY

The data that support the findings of this study are available from the corresponding author upon reasonable request.

[1] P. REICHL, K. HOURIGAN, and M. C. THOMPSON, "Flow past a cylinder close to a free surface," Journal of Fluid Mechanics **533**, 269–296 (2005).

[2] L. Prahl, A. Hölzer, D. Arlov, J. Revstedt, M. Sommerfeld, and L. Fuchs, "On the interaction between two fixed spherical particles," International Journal of Multiphase Flow **33**, 707–725 (2007).

[3] L. Prahl, A. Jadoon, and J. Revstedt, "Interaction between two spheres placed in tandem arrangement in steady and pulsating flow," International Journal of Multiphase Flow **35**, 963–969 (2009).

[4] H. R. Díaz-Ojeda, F. J. Huera-Huarte, and L. M. González-Gutiérrez, "Hydrodynamics of a rigid stationary flat plate in cross-flow near the free surface," Physics of Fluids **31**, 102108 (2019), https://doi.org/10.1063/1.5111525.

[5] A. Okajima, "Numerical simulation of flow around rectangular cylinders," **33**, 171–180.

[6] H. Díaz-Ojeda, L. González, and F. Huera-Huarte, "On the influence of the free surface on a stationary circular cylinder with a flexible splitter plate in laminar regime," Journal of Fluids and Structures **87**, 102–123 (2019).

[7] P. Niegodajew, P. Procházka, V. Uruba, W. Elsner, and R. Gnatowska, "Effect of the angle of attack on the flow around two non-identical-height square buildings in tandem arrangement," **248**, 111076.

[8] L. Schickhofer and H. Hanson, "Aerodynamic effects and performance improvements of running in drafting formations," **122**, 110457.

[9] E. Achenbach, "Vortex shedding from spheres," Journal of Fluid Mechanics **62**, 209–221 (1974).

[10] I. Nakamura, "Steady wake behind a sphere," The Physics of Fluids **19**, 5–8 (1976), https://aip.scitation.org/doi/pdf/10.1063/1.861328.

[11] S.-B. Wen and C.-L. Lai, "Theoretical analysis of flow passing a single sphere moving in a micro-tube," **459**, 495–526.

[12] D. A. R. Jones and D. B. Clarke, "Simulation of flow past a sphere using the fluent code,".

[13] S. Taneda, "Experimental investigation of the wake behind a sphere at low reynolds numbers," Journal of the Physical Society of Japan **11**, 1104–1108 (1956), https://doi.org/10.1143/JPSJ.11.1104.

[14] R. H. Magarvey and R. L. Bishop, "Transition ranges for three-dimensional wakes," Canadian Journal of Physics **39**, 1418–1422 (1961), https://doi.org/10.1139/p61-169.

[15] J.-S. Wu and G. M. Faeth, "Sphere wakes in still surroundings at intermediate reynolds numbers," AIAA Journal **31**, 1448–1455 (1993), https://doi.org/10.2514/3.11794.

[16] S. Lee, "A numerical study of the unsteady wake behind a sphere in a uniform flow at moderate reynolds numbers," Computers & Fluids **29**, 639–667 (2000).

[17] I. Kim and A. J. Pearlstein, "Stability of the flow past a sphere," Journal of Fluid Mechanics **211**, 73–93 (1990).

[18] R. Natarajan and A. Acrivos, "The instability of the steady flow past spheres and disks," Journal of Fluid Mechanics **254**, 323–344 (1993).

[19] A. G. TOMBOULIDES and S. A. ORSZAG, "Numerical investigation of transitional and weak turbulent flow past a sphere," Journal of Fluid Mechanics **416**, 45–73 (2000).

[20] T. A. JOHNSON and V. C. PATEL, "Flow past a sphere up to a reynolds number of 300," Journal of Fluid Mechanics **378**, 19–70 (1999).

[21] H. Sakamoto and H. Haniu, "A Study on Vortex Shedding From Spheres in a Uniform Flow," Journal of Fluids Engineering **112**, 386–392 (1990).

[22] J. Li and B. Zhou, "The symmetry and stability of the flow separation around a sphere at low and moderate reynolds numbers," Symmetry **13** (2021), 10.3390/sym13122286.

[23] H. Sakamoto and H. Haniu, "The formation mechanism and shedding frequency of vortices from a sphere in uniform shear flow," Journal of Fluid Mechanics **287**, 151–171 (1995).

[24] R. Mittal, "Planar symmetry in the unsteady wake of a sphere," AIAA Journal **37**, 388–390 (1999), https://doi.org/10.2514/2.722.

[25] U. Dallmann, H. Gebing, and H. Vollmers, "Unsteady three-dimensional separated flows around a sphere - analysis of vortex chain formation," in *Bluff-Body Wakes, Dynamics and Instabilities*, edited by H. Eckelmann, J. M. R. Graham, P. Huerre, and P. A. Monkewitz (Springer Berlin Heidelberg, Berlin, Heidelberg, 1993) pp. 27–30.

[26] S. Kim and P. V. Arunachalam, "The general solution for an ellipsoid in low-reynolds-number flow," **178**, 535–547.

[27] C.-C. Chang, B.-H. Liou, and R.-L. Chern, "An analytical and numerical study of axisymmetric flow around spheroids," **234**, 219–246.

[28] A. Blanco and J. Magnaudet, "The structure of the axisymmetric high-Reynolds number flow around an ellipsoidal bubble of fixed shape," **7**, 1265–1274.

[29] C.-Y. Tsai and A. Whitney, "Numerical study of three-dimensional flow separation for a 6:1 ellipsoid," in *37th Aerospace Sciences Meeting and Exhibit*, https://arc.aiaa.org/doi/pdf/10.2514/6.1999-172.

[30] J. H. Masliyah and N. Epstein, "Numerical study of steady flow past spheroids," **44**, 493–512.

[31] A. Gross, A. Kremheller, and H. Fasel, "Simulation of flow over suboff bare hull model," in *49th AIAA Aerospace Sciences Meeting including the New Horizons Forum and Aerospace Exposition*, https://arc.aiaa.org/doi/pdf/10.2514/6.2011-290.

[32] A. Ashok, T. Van Buren, and A. Smits, "Asymmetries in the wake of a submarine model in pitch," **774**, 416–442.

[33] J. Li and B. Zhou, "Vortex shedding, flow separation, and drag coefficient in the flow past an ellipsoid of different aspect ratios at moderate Reynolds number," **12**, 055202, https://pubs.aip.org/aip/adv/article-pdf/doi/10.1063/5.0090735/16464766/055202_1_online.pdf.

[34] G. K. El Khoury, H. I. Andersson, and B. Pettersen, "Wakes behind a prolate spheroid in crossflow," **701**, 98–136.

[35] C. E. Costis, N. T. Hoang, and D. P. Telionis, "Laminar separating flow over a prolate spheroid," **26**, 810–816, https://doi.org/10.2514/3.45845.

[36] N. A. N Wikström, U Svennberg and C. Fureby, "Large eddy simulation of the flow around an inclined prolate spheroid," **5**, N29, https://www.tandfonline.com/doi/pdf/10.1088/1468-5248/5/1/029.

[37] G. Constantinescu, H. Pasinato, Y.-Q. Wang, and K. Squires, "Numerical investigation of flow past a prolate spheroid," in *40th AIAA Aerospace Sciences Meeting & Exhibit*, https://arc.aiaa.org/doi/pdf/10.2514/6.2002-588.

[38] T. C. Fu, A. Shekarriz, J. Katz, and T. T. Huang, "The flow structure in the lee of an inclined 6:1 prolate spheroid," **269**, 79–106.

[39] S. AHN and R. SIMPSON, "Cross-flow separation on a prolate spheroid at angles of attack," in *30th Aerospace Sciences Meeting and Exhibit*, https://arc.aiaa.org/doi/pdf/10.2514/6.1992-428.

[40] H. Andersson, F. Jiang, and V. Okulov, "Instabilities in the wake of an inclined prolate spheroid," pp. 311–352.

[41] D. Sumner, "Two circular cylinders in cross-flow: A review," **26**, 849–899.

[42] J. MENEGHINI, F. SALTARA, C. SIQUEIRA, and J. FERRARI, "Numerical simulation of flow interference between two circular cylinders in tandem and side-by-side arrangements," **15**, 327–350.

[43] G. V. PAPAIOANNOU, D. K. P. YUE, M. S. TRIANTAFYLLOU, and G. E. KARNIADAKIS, "Three-dimensionality effects in flow around two tandem cylinders," **558**, 387–413.

[44] G. F. Eveson, E. W. Hall, and S. G. Ward, "Interaction between two equal-sized equal-settling spheres moving through a viscous liquid," British Journal of Applied Physics **10**, 43 (1959).

[45] J. Happel and R. Pfeffer, "The motion of two spheres following each other in a viscous fluid," AIChE Journal **6**, 129–133 (1960), https://aiche.onlinelibrary.wiley.com/doi/pdf/10.1002/aic.690060125.

[46] Y. Tsuji, Y. Morikawa, and K. Terashima, "Fluid-dynamic interaction between two spheres," International Journal of Multiphase Flow **8**, 71–82 (1982).

[47] L. Schouveiler, A. Brydon, T. Leweke, and M. Thompson, "Interactions of the wakes of two spheres placed side by side," European Journal of Mechanics - B/Fluids **23**, 137–145 (2004), bluff Body Wakes and Vortex-Induced Vibrations.

[48] V. D. Duong, V. D. Nguyen, V. T. Nguyen, and I. L. Ngo, "Low-Reynolds-number wake of three tandem elliptic cylinders," **34**, 043605, https://pubs.aip.org/aip/pof/article-pdf/doi/10.1063/5.0086685/16608891/043605_1_online.pdf.

[49] H. Versteeg and W. Malalasekera, *An Introduction to Computational Fluid Dynamics: The Finite Volume Method* (Pearson Education Limited, 2007).

[50] F. Moukalled, L. Mangani, and M. Darwish, *The Finite Volume Method in Computational Fluid Dynamics: An Advanced Introduction with OpenFOAM and Matlab*, 1st ed. (Springer Publishing Company, Incorporated, 2015).

[51] J. Oro, *Técnicas numéricas en ingeniería de fluidos: Introducción a la dinámica de fluidos computacional (CFD) por el método de volúmenes fini-*

tos (Editorial Reverte, 2012).

[52] G. Constantinescu and K. Squires, "Les and des investigations of turbulent flow over a sphere," in *38th Aerospace Sciences Meeting and Exhibit*, https://arc.aiaa.org/doi/pdf/10.2514/6.2000-540.

[53] A. Kumar, S. Tiwari, and S. Das, "Effect of size and spacing on the wake characteristics of two spheres placed in tandem," Physics of Fluids **35** (2023).